



This is a post-refereeing final draft. When citing, please refer to the published version:

Di Prima, S., Winarski, T., Angulo-Jaramillo, R., Stewart, R.D., Castellini, M., Abou Najm, M.R., Ventrella, D., Pirastru, M., Giadrossich, F., Lassabatere, L., 2020. Detecting infiltrated water and preferential flow pathways through time-lapse ground-penetrating radar surveys. *Science of the Total Environment*. <https://doi.org/10.1016/j.scitotenv.2020.138511>



Detecting infiltrated water and preferential flow pathways through time-lapse ground-penetrating radar surveys

Simone Di Prima ^{a,b,*}, Thierry Winiarski ^b, Rafael Angulo-Jaramillo ^b, Ryan D. Stewart ^c, Mirko Castellini ^d, Majdi R. Abou Najm ^e, Domenico Ventrella ^d, Mario Pirastru ^a, Filippo Giadrossich ^a, Giorgio Capello ^f, Marcella Biddoccu ^f and Laurent Lassabatere ^b

^a Agricultural Department, University of Sassari, Viale Italia, 39, 07100 Sassari, Italy.

^b Univ Lyon, Université Claude Bernard Lyon 1, CNRS, ENTPE, UMR 5023 LEHNA, F-69518, Vaulx-en-Velin, France.

^c School of Plant and Environmental Sciences, Virginia Polytechnic Institute and State University, Blacksburg, VA, United State.

^d Council for Agricultural Research and Economics-Agriculture and Environment Research Center (CREA-AA), Via Celso Ulpiani 5, 70125 Bari, Italy.

^e Department of Land, Air and Water Resources, University of California, Davis, CA 95616, United States.

^f Institute for Agricultural and Earthmoving Machines (IMAMOTER), National Research Council of Italy, 10135 Torino, Strada delle Cacce, 73, Italy.

* Corresponding Author. E-mail: sdiprima@uniss.it

Abstract

The objective of this paper was to identify the incidence and extent of preferential flow at two experimental areas located in Lyon, France. We used time-lapse ground-penetrating radar (GPR) surveys in conjunction with automatized single-ring infiltration experiments to create three-dimensional (3D) representations of infiltrated water. In total we established three 100 cm × 100 cm GPR grids and used differenced radargrams from pre- and post-infiltration surveys to detect wetting patterns. The analyzed time-lapse GPR surveys revealed the linkage between nonuniform flow and heterogeneous soil structures and plant roots. At the first experimental area, subsurface coarse gravels acted as capillary barriers that concentrated flow into narrow pathways via funneled flow. At the second experimental area, the interpolated 3D patterns closely matched direct observation of dyed patterns, thereby validating the applied protocol. They also highlighted the important role of plant roots in facilitating preferential water movement through the subsurface. The protocol presented in this study represents a valuable tool for improving the hydraulic characterization of highly heterogeneous soils, while also alleviating some of the excessive experimental efforts currently needed to detect preferential flow pathways in the field.

Keywords: Nonuniform flow, GPR, Water infiltration, Wetting zone, Infiltrometer, Non-Newtonian fluid.

1. Introduction

Infiltration basins are increasingly used in urban areas for flood protection, groundwater recharge, and stormwater disposal (Fletcher et al., 2015). To ensure sufficient infiltration capacity, these structures are usually established over highly permeable and strongly heterogeneous soils. Water treatment can also occur when mobile contaminants become filtered and sorbed by the soil. However, the filtration capacity of infiltration basins can be strongly affected by the occurrence of preferential flow (PF) pathways (Ben Slimene et al., 2017), making it important to detect the presence of PF, its effect on infiltration, and related risks for groundwater contamination. Developing non-invasive and easily replicable procedures to study infiltration processes and the occurrence of PF pathways is crucial for assessing hydraulic functioning of infiltration basins and other soil-based green infrastructure.

Currently, PF pathways are identified either by using invasive techniques (e.g., Abou Najm et al., 2010; Stewart et al., 2014) or by direct observation of disturbed soil profiles. Dye-staining, using compounds such as uranine, brilliant blue FCF, or methylene blue, can reveal PF pathways (e.g., Alaoui et al., 2011; Kodešová et al., 2012; Kung, 1990; Luo et al., 2019; Weiler and Naef, 2003). The dyes can be sprinkled onto the soil surface (Gerke et al., 2015) or injected during infiltration experiments (Sander and Gerke, 2007), for instance with the help of

infiltrimeters (Cey and Rudolph, 2009). However, an adequate observation of deep dye patterns requires sectioning the soil along different vertical or horizontal planes, which necessitates extensive effort and destroys the soil in the process. Moreover, dye-staining often only reveals preferential pathways that are directly connected to the source (Beven and Germann, 2013). Other investigations have used different tracers, such as ¹⁸O-enriched water or bromide, to get an insight on PF (e.g., Ahuja et al., 1995; Angulo-Jaramillo et al., 2000; Jardine et al., 1989; Köhne and Gerke, 2005). These approaches require the collection of multiple samples in time and space to get information on tracer distribution within the porous medium, thus providing only discrete information about the tracer concentrations.

Ground-penetrating radar (GPR) surveys constitute a valid alternative to these traditional methods for characterizing PF paths. For the purposes of GPR, the soil may be thought of as an ensemble of multiple homogeneous regions with contrasting electromagnetic properties (e.g., dielectric permittivity, electrical conductivity), that are separated by interfaces. A GPR system sends into the soil a pulse of high-frequency electromagnetic waves (radiowaves) which oscillate near a particular frequency. When radiowaves come into contact with an interface, portions of the incoming radiowaves are reflected, transmitted and refracted. A GPR system thus allows the user to

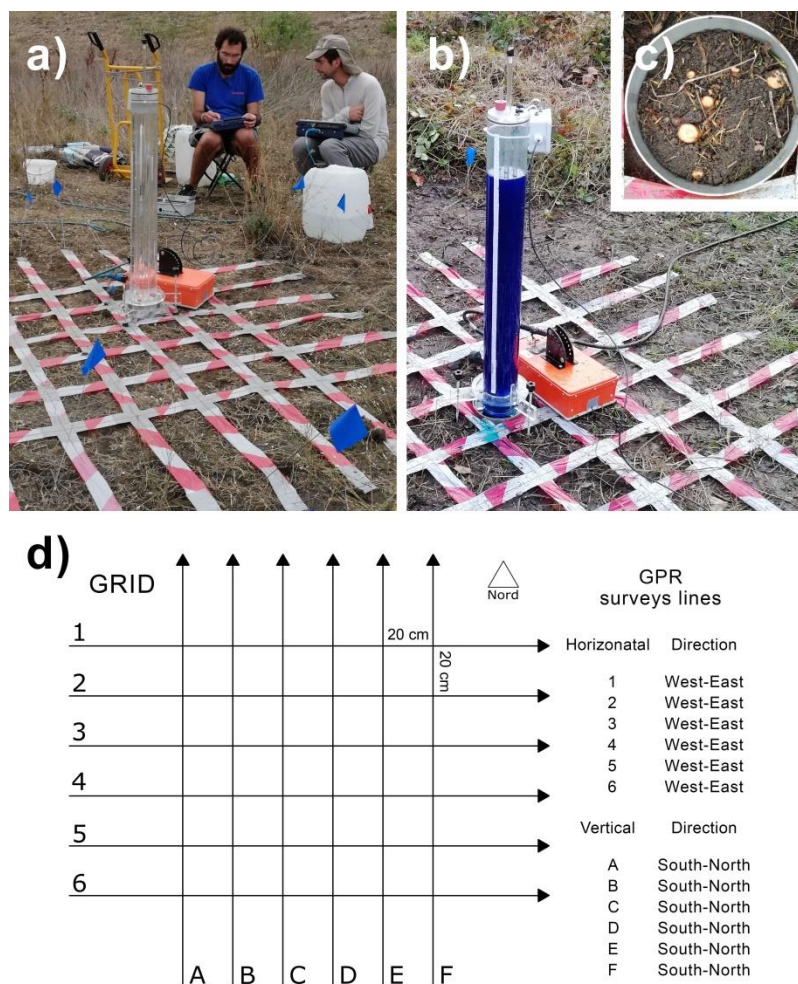


Figure 1. Experimental setup at the (a) Django Reinhardt infiltration basin and (b) Parc de La DOUA. (c) Infiltration surface at the Parc de La DOUA established in correspondence of a hawthorn shrub after cutting its shoot system. (d) Scheme of the GPR survey lines.

identify these interfaces and thereby gain information about subsurface structures.

Water flow within the unsaturated zone causes a variation of the dielectric contrast between interfaces that alters the reflection coefficient (Truss et al., 2007). These variations are manifested as amplitude changes. Based on this principle, time-lapse three-dimensional (3D) ground-penetrating radar surveys can be used to obtain differenced radargrams from pre- and post-wetting surveys (Birken and Versteeg, 2000), which has been used to investigate links between non-uniform flow and heterogeneous soil structures. For instance, Kung and Donohue (1991) first used the GPR method to detect deep soil layers with textural discontinuities that triggered PF paths on a sandy soil. This technology allowed Harari (1996) to observe non-uniform downward water movement along more active pathways in sand dunes. Truss et al. (2007) collected two-dimensional (2D) time-lapse GPR surveys before, during, and after rainfall events. The 2D time-lapse surveys were subsequently used to create a 3D GPR dataset from which these authors derived the geometry of PF paths and wetting fronts. Guo et al. (2014) combined trench infiltration tests with time-lapse GPR surveys along parallel transects to study the subsurface hydrologic dynamic of a complex lateral PF network in a hillslope. Allroggen et al. (2015) studied the potential of time-lapse GPR surveys in conjunction with rainfall simulations and brilliant blue dye injection to improve the interpretation of soil cross-sections and wetted patterns photographed after excavating the site. Guo et al. (2020) combined time-lapse GPR surveys with another non-

invasive geophysical technique, electrical resistivity tomography (ERT), to trace stemflow infiltration and identify root-derived preferential flow beneath an American beech tree.

Similar approaches were adopted by other investigations for non-invasive monitoring of temporal and spatial distribution of water flow and PF detection (e.g., Birken and Versteeg, 2000; Guo et al., 2019; Jackisch et al., 2017; Klenk et al., 2015; Trinks et al., 2001). Most of these investigations were conducted at the hillslope scale along transect survey lines, given that PF incidence and connectivity need to be characterized at appropriate scales. However, non-uniform and preferential flow phenomena may be induced by various types of soil heterogeneity (e.g., sealed soil, multi-porosity and permeability systems, porous media of contrasting materials), and can emerge at the point scale (Angulo-Jaramillo et al., 2019). In such cases, infiltration measurements combined with time-lapse GPR surveys may allow for 3D visualization of active preferential flowpaths. However, obtaining precise 3D imaging of soil wetting at small spatial scale still remains challenging, as it requires high accuracy in GPR position during the repeated surveys (Allroggen et al., 2015).

In this investigation, we combined time-lapse GPR surveys with automatized single-ring infiltration experiments to gain insight on the occurrence of PF at two experimental sites located in Lyon, France. The sites were chosen to represent two different conditions that lead to the establishment of preferential flows: lithological heterogeneity and deeply developed root systems. The present study aimed to provide

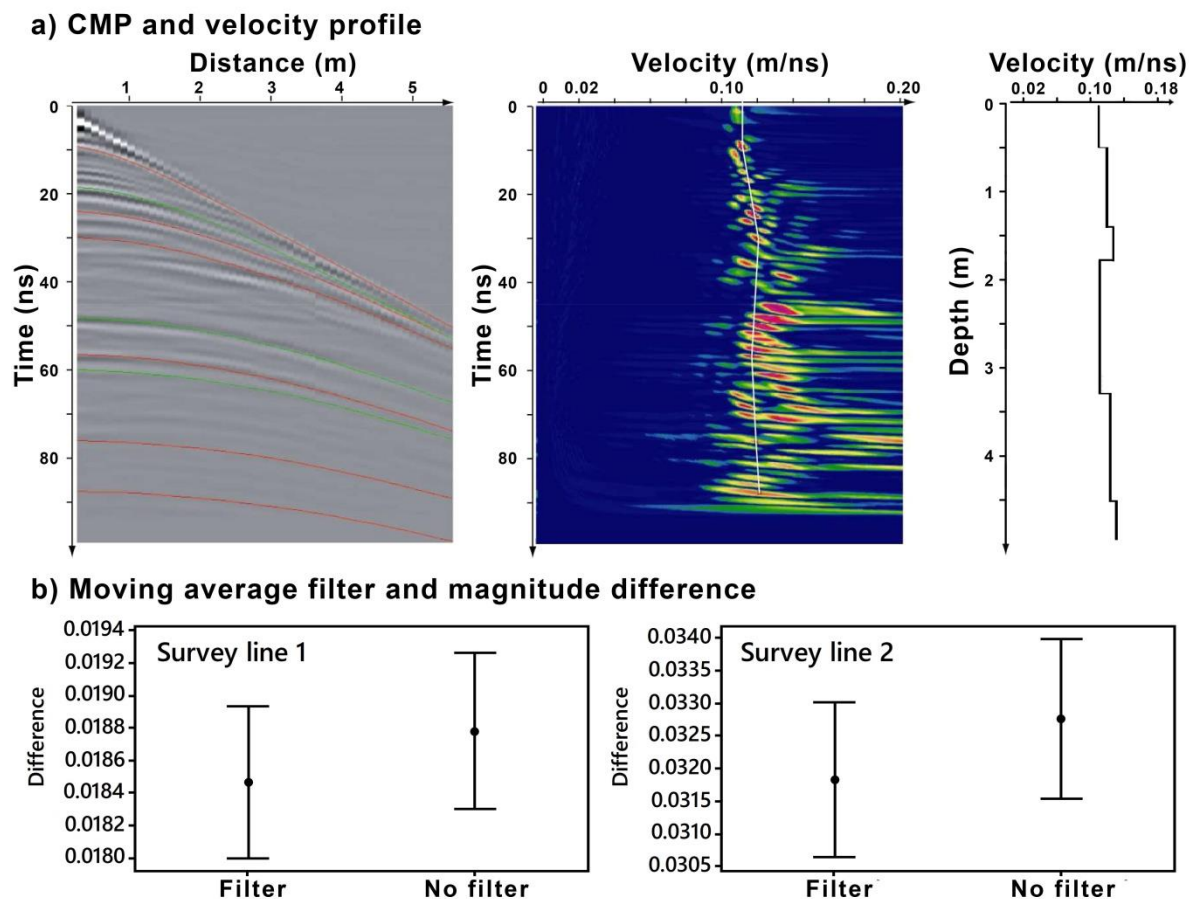


Figure 2. (a) Common-Mid-Point (CMP) determination of the velocity profile over depth (acquired in previous studies and adapted from Goutaland, 2008), and (b) comparison of the absolute differences between the pre- and post-wetting amplitudes of Survey lines 1 and 2 at the A site, with and without the filter.

experimental evidence on PF processes, with the specific objective of evaluating the ability of time-lapse GPR surveys to identify, at a small-plot scale (i.e., 100 × 100 cm), the incidence and extent of preferential flow. To achieve this objective, we used a non-invasive and easily replicable procedure to visualize the 3D wetting behaviors under ponding experiments.

2. Material and methods

2.1. Experimental areas and sampling scheme

The first field site was a stormwater infiltration basin, named Django Reinhardt basin, located in Chassieu in the eastern suburbs of Lyon, France. A detailed description of the experimental area can be found in Goutaland et al. (2008) and Winiarski et al. (2006). The infiltration basin was constructed above a heterogeneous glaciofluvial deposit by mixing together the upper 50–80 cm of the soil profile. The glaciofluvial deposit was composed of four main lithofacies: i) the uppermost mixture of the soil matrix and gravel, ii) a mixture of the soil matrix and gravel with a bimodal particle size distribution that formed most of the deposit below 50–80 cm, iii) large lenses of sand, and iv) smaller lenses of matrix-free gravel (Ben Slimene et al., 2017; Goutaland et al., 2013). Previous investigations identified how PF pathways affect groundwater quality at the studied basin, especially with regards to the transfer of pollutants (e.g., heavy metals, organics) carried by infiltrating water (Coutinho et al., 2015; Lassabatere et al., 2010, 2007, 2004). Previous modeling investigations have reported that lithological heterogeneities in the basin may induce PF, thus increasing water flux rates by more than a factor of ten compared to surface infiltration rates (Ben Slimene et al., 2017).

For the second site, the trials were carried out in an open-air flume located in an experimental garden within the La DOUA scientific campus in the municipality of Villeurbanne (France). The sampled area was colonized by ray grass and a few shrub plants with more developed root systems. The upper horizon was a mixture of matrix and gravel, 20 cm thick, under which lay a dense horizon acting as restrictive layer. The two horizons appear quite homogeneous without any lithological heterogeneity apart from layering. At the DOUA site, we determined the soil bulk density from 24 undisturbed soil cores (~ 100 cm³) collected at different depths from 0 to 50 cm (Table 1). In contrast to the first site, which was dedicated to the study of the effect of lithological heterogeneity on flow pattern, this second site was used to detect preferential flow due to plant roots in a layered profile.

Two locations (referred to as A and B) were sampled at the Django Reinhardt infiltration basin and one (referred to as DOUA) at the experimental site of “Parc de La DOUA”. At each site, a GPR grid (100 cm × 100 cm), consisting of six horizontal (1-6) and six vertical (A-F) parallel survey lines with 20 cm intervals between them, was established using white/red signaling tape (Figure 1a-b). The vertical lines were oriented along the north-south axis. Within each grid, an infiltration test was conducted. Two GPR surveys were carried out just before and then 20 min after the infiltration test. A total of 72 (3 sites × 2 GPR surveys × 12 survey lines) time-depth cross-sections (radargrams) were collected by moving the antenna along the survey lines following the sampling scheme reported in Figure 1d. Radar depth penetration and spatial resolution both vary with antenna frequency (Guo et al., 2019), so we elected to use a GSSI (Geophysical Survey System Inc., Salem, NH) SIR 3000

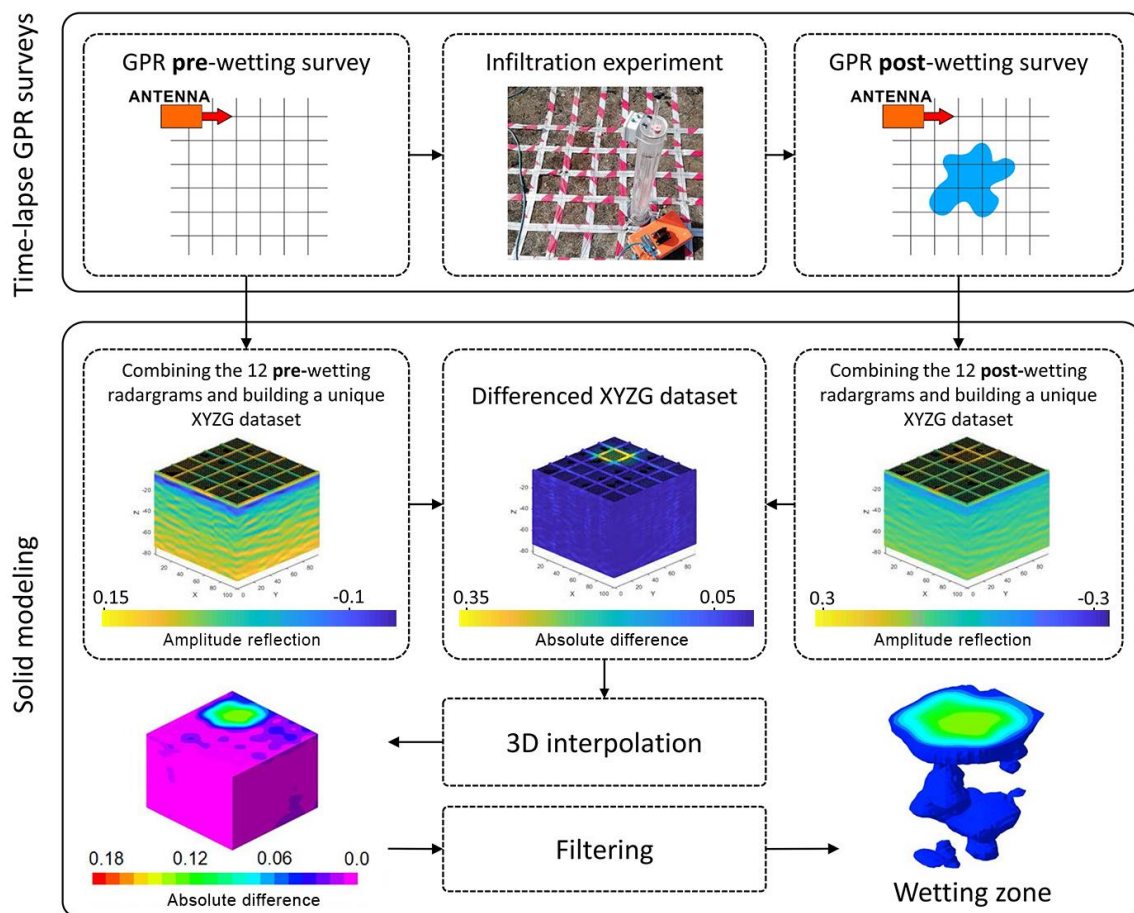


Figure 3. Flowchart illustrating the procedure to obtain the 3D diagram of the wetting zone from pre- and post-wetting ground-penetrating radar surveys.

system with a 900-MHz antenna as the best compromise between high resolution and adequate penetration for the spatial scale of our wetting experiments.

2.2. Automated ponding experiments

In this investigation, the use of dyes at the Django Reinhardt basin was restricted for operational reasons. We therefore infiltrated only water at this location. In contrast, we carried out our infiltration experiment at the DOUA site using a solution that was prepared by adding 1 g L⁻¹ of dry Xanthan gum powder and 1 g L⁻¹ of brilliant blue dye (E133) to beakers of deionized water and allowing them to mix with magnetic stirrers. The xanthan gum created a shear-thinning viscous solution that was expected to fill preferential pathways with limited infiltration into the soil matrix, and thus reveal complex geometries or macropore networks in highly heterogeneous soils (Abou Najm and Atallah, 2016; Atallah and Najm, 2019; Stewart et al., 2014). The Xanthan solution was used to boost preferential flow in the root system of the shrub plants.

At each site we used the automated single-ring infiltrometer proposed by Concialdi et al (2020) to infiltrate a volume of water corresponding to a total cumulative infiltration of 28 cm, based on an infiltration surface of 94 cm² (Figure 1a-b). We used a stainless steel ring with a 15-cm inner diameter inserted shallowly into the soil according to the Beerkan procedure for single-ring infiltration experiments (Lassabatero et al., 2006). To setup the experiment, we followed the procedure described in Di Prima (2015) and Di Prima et al. (2016). We firstly positioned a plastic film on the soil surface inside the ring and applied a small water head of 0.2-0.3 cm, depending on the surface roughness. The infiltrometer was positioned inside the ring and

regulated in height so that the base was in contact with the ponded water. The Mariotte bottle was filled with the fluid, and then activated through lifting the piston, at which time data acquisition began. Finally, the infiltration experiment started when the plastic film was removed. At the DOUA site, the infiltration surface was established around the root system of hawthorn shrub after removing its shoot system (Figure 1c). At the end of the infiltration experiment, we excavated the soil to expose the dyed patterns.

The automated procedure proposed by Concialdi et al. (2020) to treat the transducer output was subsequently applied to determine the cumulative infiltration curve. A video tutorial showing the field procedure and the data processing can be viewed online (Di Prima, 2019). The use of the automatic infiltrometers in this protocol simplified the field setup, while also reducing the amount of effort needed to characterize water infiltration. During the infiltration tests the GPR antenna was maintained in a static position close to the ring with the SIR 3000 sets for point data collection (Figure 1a-b). We recorded a single scan (i.e., one complete reflected wave from transmission to reception) every one minute in order to monitor the time evolution of infiltrated water. The first ten scans, representative of the pre-wetting condition, were recorded before starting the infiltration process. The acquisition was stopped twenty minutes after the end of the test, and a picture of the infiltration bulb at the infiltration surface was taken. Then we carried out the GPR survey on the established grid. These radargrams were combined with the infiltrometer data. This coupling of information allowed us to monitor movement of water from the infiltration surface in real-time.

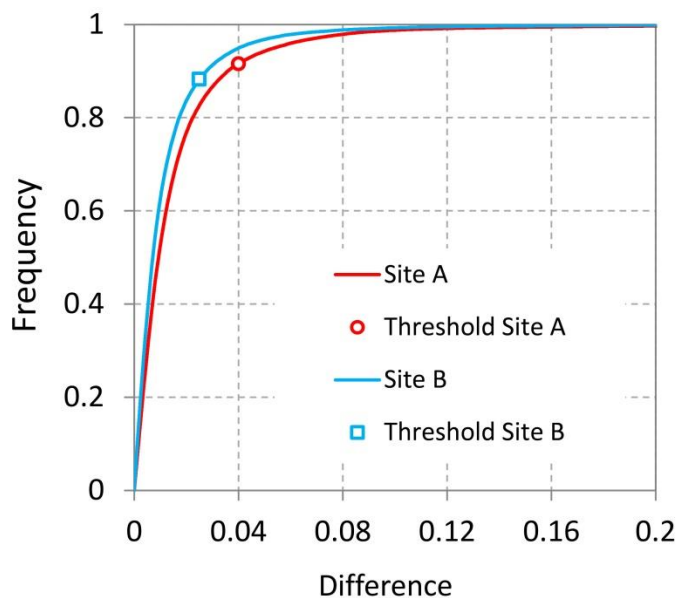


Figure 4. Cumulative frequency distributions of the absolute difference between pre- and post-wetting amplitude values for the A and B sites. The identified thresholds in amplitude differences (0.04 and 0.025) correspond to frequencies that were 1.5 times the standard deviations of each dataset.

2.3. GPR data processing and solid modeling

A GPR display typically consists of a radargram, namely a collection of time-series returns, giving a time-depth cross-sections (Al-Nuaimy et al., 2002). We processed each collected radargram using the GSSI Radan 7 software. The process consisted of distance normalization, a static time shift to align direct ground wave arrival to 0 ns, and exponential scaling to compensate GPR energy attenuation with propagation depth. In accordance with Truss et al (2007), the same gain curve (established using the pre-wetting data) was applied to all data acquired within a time-lapse series. The distance normalization allowed us to obtain an equal distance between the 20 cm marks taken along the survey line intersections.

To determine the appropriate velocity to convert two-way travel times into actual depths we relied on previous GPR-based sedimentological studies performed on the site (Goutaland et al., 2013, 2008). Those authors performed a Common-Mid-Point (CMP) acquisition to determine velocity profiles at two nearby profiles. The velocity profiles were generally uniform, with values on the order of 0.1 m ns⁻¹ (Figure 2a). In addition, the authors confirmed their estimated velocities by excavating two trenches and measuring the real distances between soil surface and several interfaces detected by the GPR, which resulted in mean values of 0.100 and 0.103 m ns⁻¹ for the two trenches (Goutaland, 2008). Based on these results, we assumed a uniform wave velocity in our analysis.

For each grid area, the amplitude values, G , from the 12 radargrams were combined to build a unique XYZG dataset, with the X, Y, and Z values representing location coordinates (easting, northing, and elevation). The elevation, Z , was determined from the wave time, given by GPR acquisition and

Table 1. Bulk density values (g cm⁻³) measured at the DOUA site.

Depth (cm)	Sample size	Min	Mean	Max
0-10	9	0.928	1.074	1.173
10-20	3	1.046	1.090	1.168
20-30	6	1.349	1.479	1.648
30-40	3	1.587	1.658	1.738
40-50	3	1.677	1.716	1.763

considering the value of wave velocity mentioned above. We therefore obtained three pre-wetting and three post-wetting XYZG datasets (Figure 3).

Next, we created three other datasets based on absolute differences between pre- and post-wetting G values. Indeed, water flowing within the unsaturated zone caused a variation of the dielectric contrast between layers that altered the reflection coefficient (Truss et al., 2007). These variations were manifested as amplitude changes. Therefore, the differenced datasets were constructed to highlight the amplitude fluctuations between repeated GPR radargrams collected over the same survey lines before and after the infiltration tests (e.g., Guo et al., 2019; Holden, 2004). We assumed that the absolute difference between the pre- and post-wetting amplitude values were negatively correlated with the soil water pressure head (Birken and Versteeg, 2000). We therefore expected strongest reflection differences in correspondence to the saturated soil bulb that extended outwards from the infiltration surface, and decreasing reflection differences in the partially saturated (transmission) zone that surrounded the wetting bulb. In this zone, the water pressure head decreases as the wetting front moves away due to soil capillarity from the saturated bulb (Angulo-Jaramillo et al., 2016). For each site, we considered all differential amplitude values greater than 1.5 standard deviations of the mean absolute amplitude for each differenced XYZG dataset to represent substantial changes in reflection due to infiltrated water. A similar criterion considering amplitudes greater than two standard deviations from the mean was used by Guo et al. (2019) to identify preferential flow through saprock. Note that we used a less strict criterion because we were interested in identifying the entire wetted soil volume.

The interpretation of differenced radargrams may be complicated by the occurrence of spurious amplitude differences due to geometrical mismatches between measurements. In addition, infiltrated water causes an increase in bulk dielectric constant, which in turn increases the travel time and lowers the reflection position, resulting in net time shifts (Truss et al., 2007). To alleviate these problems, we smoothed the radargrams by applying a moving-average filter with a window of 7 vertical time samples and 5 horizontal traces. This procedure allowed us to reduce the geometric mismatch between time-lapse survey lines, yielding lower differences between corresponding pre- and post-wetting amplitude values. A similar approach was also adopted by Guo et al. (2014), who corrected the mismatch in the Z direction by stacking successive samples on each trace using their mean value.

In this investigation, we checked the efficiency of the moving-average filter by comparing the absolute differences between the pre- and post-wetting amplitudes of the processed and unprocessed data. Figure 2b depicts an example involving two survey lines at Site A. In this example, only Survey line 2 crosses the infiltration bulb. Consequently, for this survey line the amplitude values substantially increased after the infiltration of water. That is the reason why the magnitudes scored approximately 0.0318 for Survey Line 2 (impacted by the infiltration bulb) versus 0.0185 for Survey Line 1 (less impacted by the infiltration bulb). However, in both cases, the moving-average filter reduced the difference in amplitude, with a shift from 0.0328 to 0.0318 for Survey Line 2, and 0.0188 to 0.0185 for Survey Line 1 (Figure 2b). In both cases, the mismatch

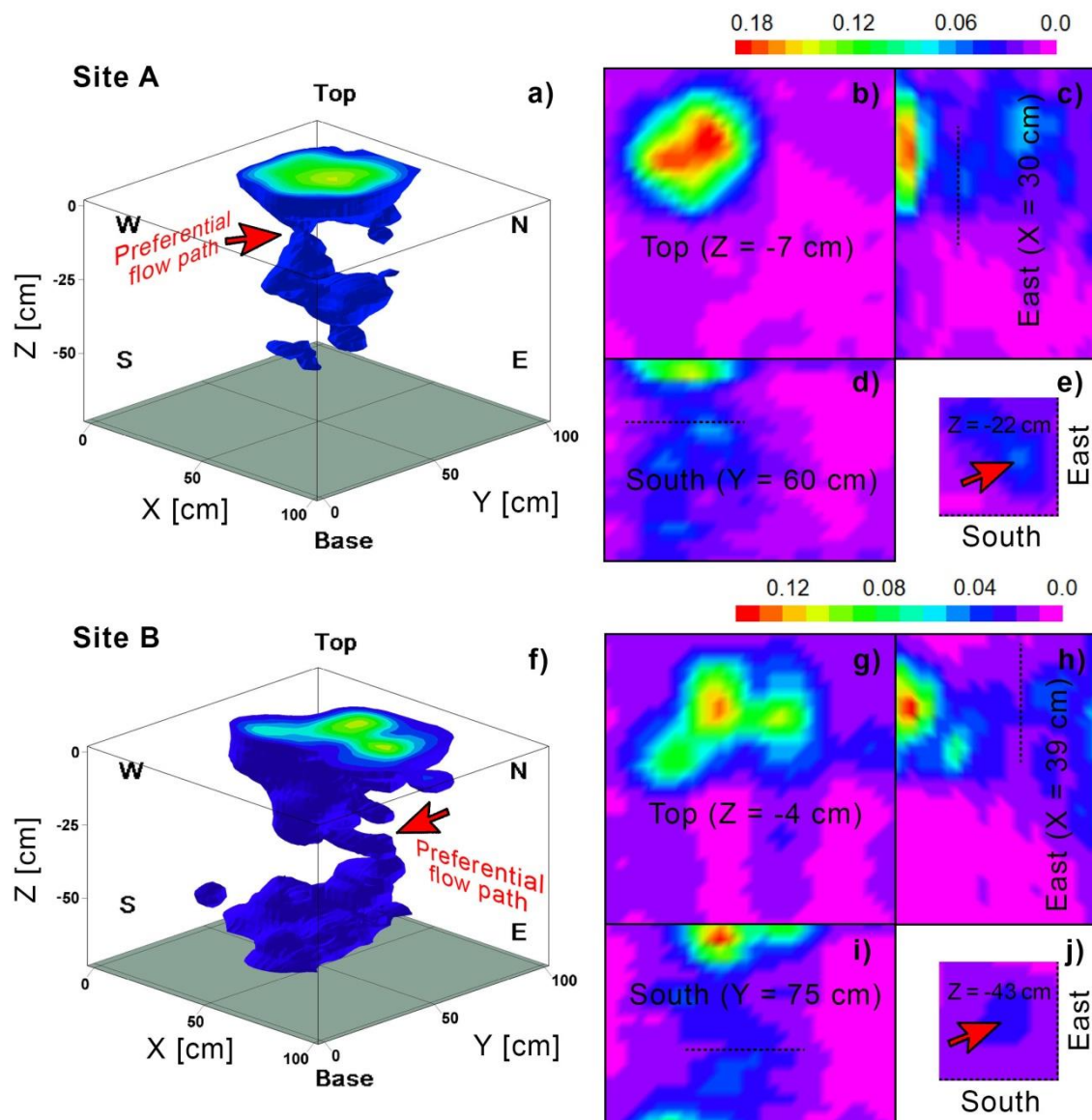


Figure 5. (a), (f): Three-dimensional representation of the wetting zones at Sites A and B. (b), (e), (g), (j): Horizontal slices extracted from the 3D diagrams at different depths from the soil surface. (c), (h): North-south oriented (east view) and (d), (i): West-east oriented (south view) vertical slices. Red arrows highlight the detected preferential flow pathways. Colors scales indicate the absolute difference between pre- and post-wetting amplitude values. A video included as supplementary material shows a 360-degree view of wetting zone at Site A.

correction was effective, yielding smaller differences between pre- and post-wetting. Based on this finding, we were confident that this process reduced the difference in amplitude that resulted from the time shift induced by the change of velocity with wetting, while keeping the difference in amplitude that resulted from the change in water content.

We used the RockWorks 17 software (RockWare, Inc., 2015) and the inverse-distance anisotropic modeling method to perform a 3D interpolation of the differenced datasets. This type of directional search can improve the interpolation of voxel (volumetric picture element) values that lie between data point clusters, and it has been applied in different geophysical investigations (e.g., Attwa and El-Shinawi, 2017; Lange-Athinodorou et al., 2019; Longo et al., 2014). Here, the method assigned a voxel node value on the basis of the weighted average of neighboring data points looking in each 90-degree sector around the node. The amplitude value of each data point was weighted according the inverse of its distance from the voxel node, taken to a power of 2 (inverse-distance squared).

3. Results and discussion

3.1. Determination of the 3D representation of wetted zones

The GPR determination of the wetted zone is illustrated for the Django Reinhardt site. The absolute differences between the pre- and post-wetting amplitude values ranged from 0 to 0.394 for Site A and from 0 to 0.293 for Site B. According to our stated criterion (i.e., amplitude values greater than 1.5 standard deviations), the estimated thresholds used to filter the differenced XYZG datasets were equal to 0.04 (Site A) and 0.025 (Site B), which corresponded to cumulative frequencies of 0.92 and 0.88 (Figure 4). Thus, only 8 to 12% of the amplitude values measured by the radargrams showed substantial changes between pre- and post-wetting.

After filtering, 3D interpolation was used to visualize and quantify the wetted soil volumes associated with each infiltration experiment. The 3D diagrams clearly demarcated the dimensions and shapes of the wetted zones created during both experiments (Figures 5a and f). Then, we compared these

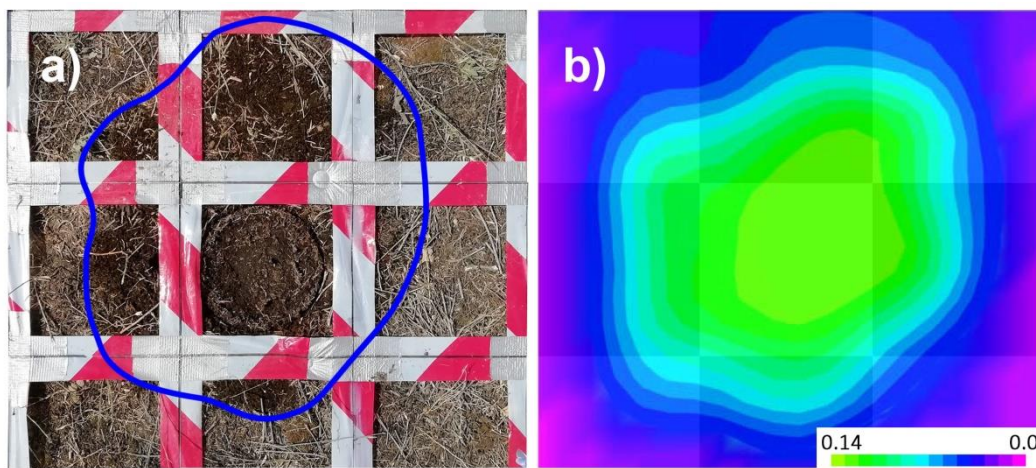


Figure 6. Comparison between (a) the infiltration bulb observed at the end of the experiment (delineated on the picture) and (b) the wetted zone identified by GPR survey at the soil surface for Site A.

demarcated wetted zones with the observations of the infiltration bulbs at the soil surface at the end of the experiment. **Figure 6** illustrates the comparison between the observed infiltration bulb at the surface (**Figure 6a**, delineated on the picture) and the expansion of the wetted zone in the 3D diagram at the soil surface (**Figure 6b**), based on results from Site A. Similar results were obtained for Site B. The correspondence between the two shapes constituted a first encouraging signal of the validity of the 3D interpolation procedure to determine the wetted pattern at the soil surface. However, dye-staining results obtained at the DOUA site better supported the use of GPR to identify 3D wetting patterns, as discussed in the next section.

Both experiments had hemispherical-shaped wetted zones in the upper soil horizon that extended to depths of approximately 20 cm (**Figure 5**: Site A in subpanels c-d and Site B in subpanels h-j). In this hemispherical zone, infiltration was mainly controlled by the matrix, resulting in a uniform distribution of water. Below this upper layer, the wetting patterns became vertically elongated and irregularly shaped. As discussed in the next section, these patterns were assumed to be associated with PF paths (Regalado et al., 2005). The estimated volumes of the wetted zones were 48.1 L (Site A) and 72.8 L (Site B), with the second volume characterized by lower reflection changes (**Figure 7**). Given that identical volumes of water infiltrated during the tests at both locations, we argue that the expansion of the wetting front due to capillary forces was more relevant at Site B, yielding a larger volume of wetted soil with a smaller degree of wetting (Moncef et al., 2002).

3.2. Detection of preferential flow pathways

At the DOUA site, dyed zones were observed after excavating the soil (**Figure 8**). The use of time-lapse GPR surveys in conjunction with staining-dye tracer allowed us to verify the 3D interpolation procedure. The GPR data resolved water perching above a shallow restrictive layer (demarcated zone Z1 in **Figure 8a-c**), which was confirmed by the concentration of dye at that interface (**Figure 8c**). Below this layer, the 3D diagram showed elongated and irregularly shaped wetting patterns (demarcated zones Z2 and Z3 in **Figure 8a-b**), which corresponded with roots present at 30 and 40 cm depths (demarcated zones Z2 and Z3 in **Figure 8c**). The GPR data and dye staining patterns therefore both indicated that water

infiltrated through this restrictive layer mainly following the plant root system, revealing that roots act as important flow pathways at the studied site.

At the Django Reinhardt basin, the use of dyes was restricted for operational reasons; thus, the main PF paths were firstly identified from the 360-degree view of the wetted zones. Then, horizontal and vertical slices were extracted from the 3D diagrams to identify zones with strong reflection differences corresponding to patches of wetted soil located below the main wetting front (**Figure 5**: Site A in subpanels c-e and Site B in subpanels h-j; also shown in a video included as [supplementary material](#)). The slices were then overlapped with the pre-wetting radargrams to identify the source of spatial heterogeneity that triggered PF. In both sites, subsurface coarse gravels with low capillarity, and thus low unsaturated hydraulic conductivity (Goutaland et al., 2013), acted as capillary barriers that concentrated flow into relatively narrow pathways (**Figure 9**), in a process commonly referred to as funneled flow (Kung, 1990). In Site A, the 3D diagram showed that flow channeling occurred at a depth of 22 cm. In the underlying horizons the soil had finer soil textures and likely greater capillary forces, which encouraged lateral spreading of the wetting front. In Site B, the 3D diagram showed that flow channeling occurred at a depth of 43 cm. The wetting front exceeded the maximum soil depth sampled by GPR surveys in Site B (70 cm). As a result, the wetted soil volume was likely underestimated at this location.

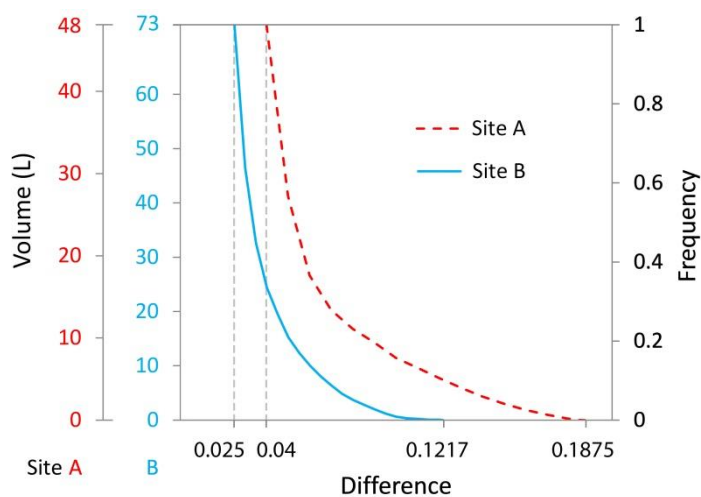


Figure 7. Volumes of the wetted zones for Sites A and B (left Y-axis) and associated cumulative frequency distributions (right Y-axis) of the interpolated values that define the colour ranges of the solid diagrams.

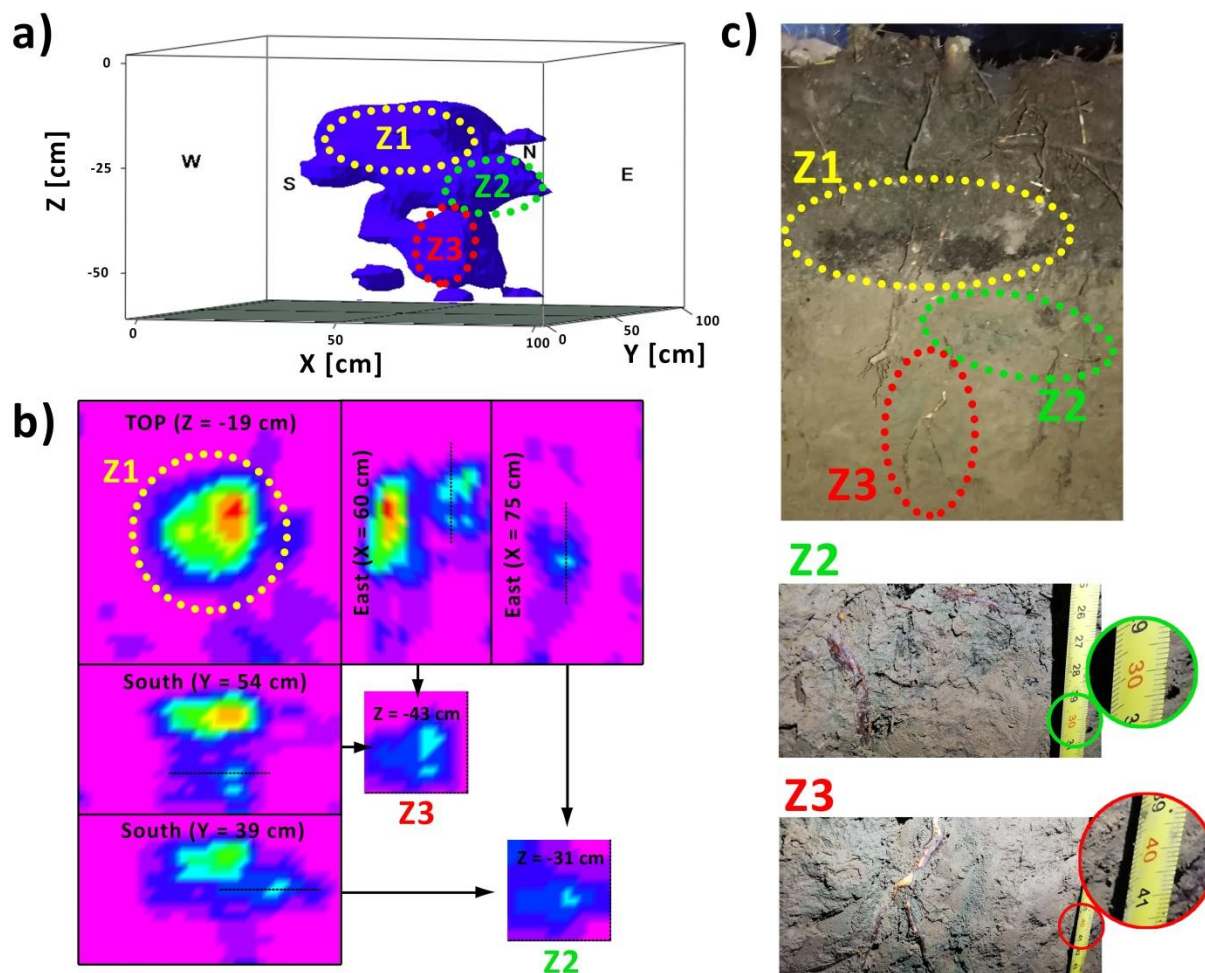


Figure 8. (a): Three-dimensional representation of the wetting zones at the DOUA site. (b): Horizontal and vertical slices extracted from the 3D diagrams. (c): Picture of the soil profile excavated after the post-wetting GPR survey. The green and red demarcated zones Z2 and Z3 highlight bypass flow within the plant root system. The yellow demarcated zone Z1 highlights the accumulation of water within the interface of the two layers.

3.3. Real time monitoring of infiltration at surface (GPR punctual acquisition)

We also analyzed the ability of GPR punctual acquisition to provide real-time monitoring of infiltration processes from the soil surface. Our first finding here was that no clear information is provided when the wetting bulb is too small to be detected by the antenna. That was the case of the location B of the Django Reinhardt site. The wetted zone here expanded mainly in the southeast direction, far from the position of the antenna (which was located northwest side of the ring). Consequently, the point GPR measurements collected during the infiltration test at that site did not provide clear evidence of water flow.

However, we measured substantial reflection changes below the antenna position during the infiltration test at Site A, where initial infiltration rates were relatively low before starting to increase ~2 minutes after the start of the experiment (Figure 10). The resultant cumulative infiltration curve exhibited a convex shape typically associated with soil water repellency (Alagna et al., 2018; Di Prima et al., 2019; Lassabatere et al., 2019a). This infiltration impedance caused a delayed response of reflection changes, which were initially detected 3 minutes after infiltration started (Figure 10a). In addition, the antenna was positioned at the northwest edge of the infiltrometer, so detection was possible only after sufficient lateral expansion of the wetted zone. At the end of the infiltration test (i.e., at time =

18 min), a strong increase in signal amplitude appeared at approximate depths of 50 and 70 cm, indicating the wetting zone reached the lower boundary of 70 cm (Figure 10a). After that, drainage and water redistribution rates diminished and the water profile approached hydrostatic conditions, as signaled by constant amplitudes for the final 15 minutes of the measurement. Because the wetted zone did not change in shape and dimension at the end of the infiltration run, we assume that water drainage and redistribution was slow enough to allow proper acquisition of GPR over the complete grid survey. In other words, the last GPR acquisition (last Survey line) described the same soil moisture condition than the first survey line. Consequently, all survey lines described the same wetted zone and can be concatenated to form a 3D representation of the entire wetted zone.

GPR punctual acquisition and time-lapse GPR (3D block) were cross-checked. At the end of the measurement, we identified the depth of the stronger signal amplitudes in the final scans of the radargram (Figure 10a). We subsequently extracted horizontal slices from 3D diagram at the corresponding depths (Figure 10b). There was a perfect agreement between stronger signal amplitudes and the occurrence of deep wetter patches positioned vertically below the antenna. These observations increased our confidence in the 3D interpolation procedure that was previously performed to determine the wetted zone volume.

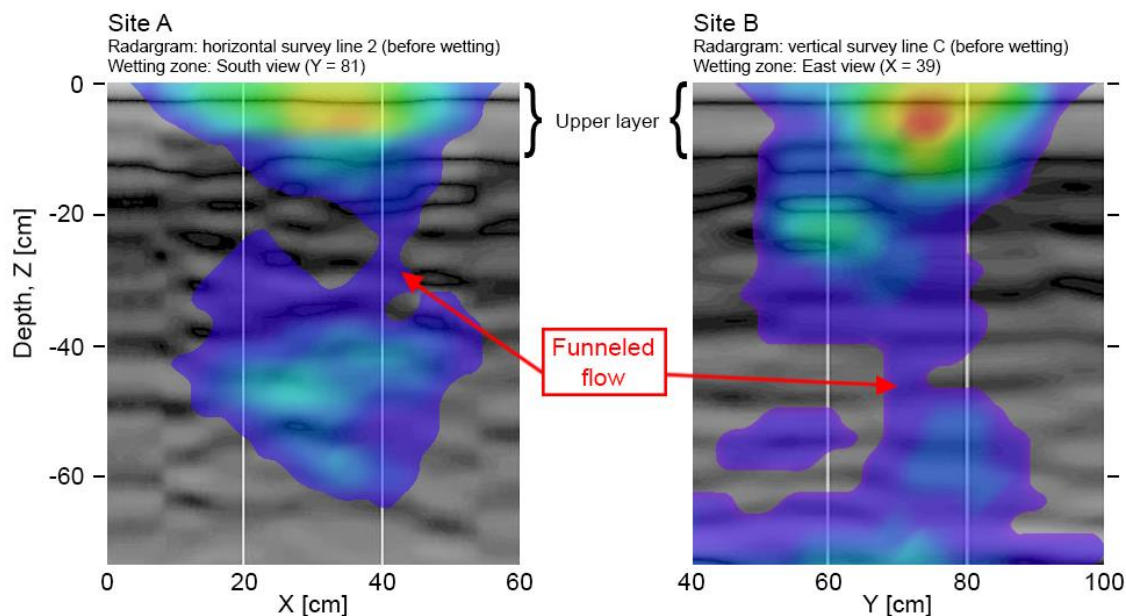


Figure 9. Overlapping of selected vertical slices extracted from 3D diagrams with the pre-wetting radargrams. Red arrows highlight the detected preferential funneled flow.

4. Discussion

The use of time-lapse GPR surveys in conjunction with staining-dye tracer at the DOUA site allowed us to verify the 3D interpolation procedure. Here the comparison confirmed that the GPR was able to accurately resolve perched water above a shallow restrictive layer along with deeper preferential flow associated with a shrub plant root system (Figure 8). That pattern is in line with the expected water infiltration in layered systems and with the potential role of leaks by the plant root systems in layered soils (Gerke et al., 2015). However, the wetted zones detected by the GPR in the vicinity of the root system were larger than the zones visibly stained with dye. Further investigations are thus needed to better understand the dimensions of flow pathways detectable with GPR, including whether the technology is able to resolve very small fingers or pores.

For the Django Reinhardt site, we observed a uniform distribution of water with hemispherical-shaped wetted zones in the upper layer where the soil matrix controlled water flow, and vertically elongated and irregularly shaped wetting patterns corresponding to the coarse gravels below. Therefore, the 3D observation of the wetted zones using GPR allowed the detection of preferential funneled flow due to lithological heterogeneities. This result can be viewed as an experimental confirmation of previous modeling investigations carried out at the same infiltration basin by Coutinho et al. (2015) and Ben Slimene et al. (2017). The latter study speculated that lithological heterogeneities in the basin (e.g., the subsurface gravel lenses) may induce funneled flow, so the present study provides experimental evidence showing that this process does commonly occur (as we observed PF at both tested locations). Moreover, the 3D diagrams provided additional insight into spatial differences in PF processes. Here, the depth of funneled flow varied between locations in the same site, as did the subsequent shape, volume, and depth of wetting in the finer-textured underlying soil. The two infiltration tests introduced nearly identical volumes of water into the soil, so the GPR scans

were crucial to identify actual differences in infiltration and flow pathways.

Our findings clearly show that GPR can be used for the detection for preferential flow and to get a picture of water pathways for both cases: lithological heterogeneity and root systems. These data have notable practical applications. For example, infiltration patterns measured at the surface of a stratified medium are often influenced by hydraulic behaviors of any restrictive layers, yet infiltration data alone typically do not contain sufficient information to characterize different layers. This limitation was identified by Lassabatere et al. (2010) for the case of the sediment settlement in the Django Reinhardt basin, as well as by many authors in other locations (e.g., Alagna et al., 2019; Di Prima et al., 2018; Yilmaz et al., 2013, 2010). Similarly, when water flows simultaneously through the soil matrix and a macropore network, both flow domains contribute to the hydraulic properties of the soil (Lassabatere et al., 2019b, 2014; Stewart, 2019). Our analysis showed that non-uniform wetting patterns are detectable using GPR, so this information could be used to improve the parameterization of hydraulic properties for both homogeneous and heterogeneous soils.

One potential limitation of the applied protocol is the uncertainty associated with spurious amplitude differences. This problem depends in part on small differences of the antenna position between successive surveys. Also, the lowering of the reflection position after the increase of the water content may induce a time shift and consequently a mismatch in the vertical direction. In this investigation, we alleviated these problems, at least in part, by smoothing the radargrams both in the horizontal and vertical directions. The smoothing process proved satisfactory for removing these potential artifacts while retaining sufficient resolution to demarcate the extent and degree of wetting during localized infiltration processes. Therefore, we encourage other practitioners to employ similar techniques when using GPR-based measurements to analyze preferential wetting behaviors.

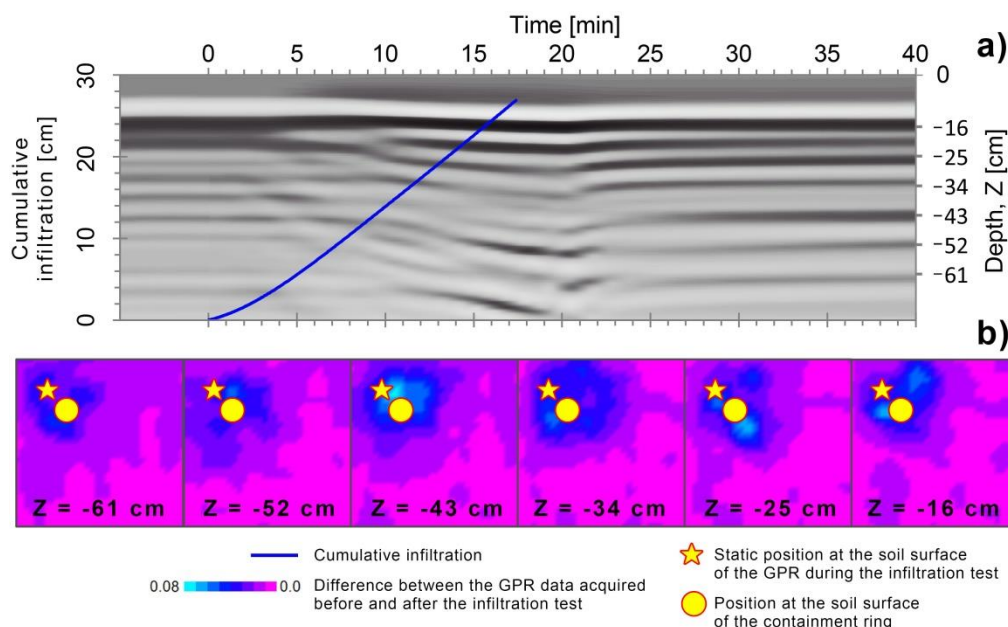


Figure 10. (a) Overlapping of the cumulative infiltration curve with the radargram measured at the A site during the infiltration test. (b) Horizontal slices extracted from the 3D diagram at depths corresponding to the strongest changes in signal amplitudes.

5. Summary and conclusions

In this study, we combined time-lapse GPR surveys with automated single-ring infiltration experiments. The proposed procedure used non-invasive monitoring of the spatial distribution of infiltrated water to create 3D representations of infiltrated water. A dye-staining experiment conducted at one of the experimental sites provided verification that the applied procedure was able to identify preferential flow caused by shrub roots. In all experimental sites, the 3D diagrams created using the proposed procedure clearly demarcated the wetting zone dimensions and shapes, and facilitated detection of preferential flow pathways and funneled flow in the subsurface. In the future such information may serve to verify hydraulic characterization procedures using water infiltration experiments, and may be particularly useful in highly heterogeneous soils, including sealed soils, multi-porosity/multi-permeability systems, and stratified profiles. Indeed, this study can be viewed as a step towards time-lapse GPR surveys becoming more widely applied in the field as a reliable and non-invasive way for investigating linkages between non-uniform flow and heterogeneous soil structures.

Funding

This work was supported through i) the INFILTRON Project (ANR-17-CE04-0010, Package for assessing infiltration & filtration functions of urban soils in stormwater management; <https://infiltron.org/>), ii) the European Regional Development Fund (ERDF) and the Italian Ministry of Education, University and Research (MIUR) through the “Programma Operativo Nazionale (PON) Ricerca e Innovazione 2014-2020 (Linea 1 - Mobilità dei ricercatori, AIM1853149, CUP: J54I18000120001), and iii) the Short Term Mobility (STM) Program 2019 of CNR (Research Programme: “Innovative techniques for hydraulic characterization of soil”).

CRedit authorship contribution statement

Simone Di Prima: Conceptualization, Funding acquisition, Methodology, Investigation, Formal analysis, Visualization, Writing - review & editing. Thierry Winiarski: Resources, Writing - review & editing. Rafael Angulo-Jaramillo: Writing - review & editing. Ryan D. Stewart: Writing - review & editing. Mirko Castellini: Writing - review & editing. Majdi R. Abou Najm: Writing - review & editing. Domenico Ventrella: Writing - review & editing. Mario Pirastru: Writing - review & editing. Filippo Giadrossich: Writing - review & editing. Giorgio Capello: Investigation, Writing - review & editing. Marcella Biddoccu: Funding acquisition, Writing - review & editing. Laurent Lassabatere: Conceptualization, Funding acquisition, Methodology, Investigation, Writing - review & editing.

Acknowledgements

The authors thank Sara Puijalon and the Lyon city Field Observatory for Urban Water Management (OTHU), for technical and scientific support, and Jean-Philippe Bedell for advices on plant root systems.

Author Contributions

S. Di Prima and L. Lassabatere outlined the investigation and carried out the field experiments at the Django Reinhardt infiltration basin. S. Di Prima and G. Capello carried out the field experiment at the DOUA site. S. Di Prima analyzed the data and created the video. All authors contributed to discussing the results and writing the manuscript.

Conflicts of interest

The authors declare that they have no known competing financial interests or personal relationships that could have appeared to influence the work reported in this paper.

Appendix A Supplementary data

Supplementary data associated with this article can be found in the online version at <https://doi.org/10.1016/j.scitotenv.2020.138511>. These data include the Google map of the most important areas described in this article and a video showing a 360-degree view of wetting zone at Site A (<https://youtu.be/pMbddiqsjd4>).

References

- Abou Najm, M.R., Atallah, N.M., 2016. Non-Newtonian Fluids in Action: Revisiting Hydraulic Conductivity and Pore Size Distribution of Porous Media. *Vadose Zone Journal* 15, 0. <https://doi.org/10.2136/vzj2015.06.0092>
- Abou Najm, M.R., Jalal D. Jabro, William M. Iversen, Rabi H. Mohtar, Robert G. Evans, 2010. New method for the characterization of three-dimensional preferential flow paths in the field. *Water Resources Research* 46. <https://doi.org/10.1029/2009WR008594>
- Ahuja, L.R., Johnsen, K.E., Heathman, G.C., 1995. Macropore Transport of a Surface-Applied Bromide Tracer: Model Evaluation and Refinement. *Soil Science Society of America Journal* 59, 1234–1241. <https://doi.org/10.2136/sssaj1995.03615995005900050004x>
- Alagna, V., Bagarello, V., Di Prima, S., Guaitoli, F., Iovino, M., Keesstra, S., Cerdà, A., 2019. Using Beerkan experiments to estimate hydraulic conductivity of a crusted loamy soil in a Mediterranean vineyard. *Journal of Hydrology and Hydromechanics* 67, 191–200. <https://doi.org/10.2478/johh-2018-0023>
- Alagna, V., Iovino, M., Bagarello, V., Mataix-Solera, J., Lichner, L., 2018. Alternative analysis of transient infiltration experiment to estimate soil water repellency. *Hydrological Processes*. <https://doi.org/10.1002/hyp.13352>
- Alaoui, A., Caduff, U., Gerke, H.H., Weingartner, R., 2011. A Preferential Flow Effects on Infiltration and Runoff in Grassland and Forest Soils. *Vadose Zone Journal* 10, 367. <https://doi.org/10.2136/vzj2010.0076>
- Allroggen, N., van Schaik, N.L.M.B., Tronicke, J., 2015. 4D ground-penetrating radar during a plot scale dye tracer experiment. *Journal of Applied Geophysics* 118, 139–144. <https://doi.org/10.1016/j.jappgeo.2015.04.016>
- Al-Nuaimy, W., Huang, Y., Shihab, S., Eriksen, A., 2002. Automatic target detection in GPR data. in: Koppenjan, S., Lee, H. (Eds.), . Presented at the Ninth International Conference on Ground Penetrating Radar (GPR2002), Santa Barbara, CA, pp. 139–143. <https://doi.org/10.1117/12.462232>
- Angulo-Jaramillo, R., Bagarello, V., Di Prima, S., Gosset, A., Iovino, M., Lassabatere, L., 2019. Beerkan Estimation of Soil Transfer parameters (BEST) across soils and scales. *Journal of Hydrology* 576, 239–261. <https://doi.org/10.1016/j.jhydrol.2019.06.007>
- Angulo-Jaramillo, R., Bagarello, V., Iovino, M., Lassabatere, L., 2016. Infiltration Measurements for Soil Hydraulic Characterization. Springer International Publishing.
- Angulo-Jaramillo, R., Vandervaere, J.-P., Roulier, S., Thony, J.-L., Gaudet, J.-P., Vauclin, M., 2000. Field measurement of soil surface hydraulic properties by disc and ring infiltrometers: A review and recent developments. *Soil and Tillage Research* 55, 1–29. [https://doi.org/10.1016/S0167-1987\(00\)00098-2](https://doi.org/10.1016/S0167-1987(00)00098-2)
- Atallah, N.M., Najm, M.R.A., 2019. Characterization of synthetic porous media using non-Newtonian fluids: experimental evidence. *European Journal of Soil Science* 70, 257–267. <https://doi.org/10.1111/ejss.12746>
- Attwa, M., El-Shinawi, A., 2017. An integrative approach for preliminary environmental engineering investigations amidst reclaiming desert-land: a case study at East Nile Delta, Egypt. *Environ Earth Sci* 76, 304. <https://doi.org/10.1007/s12665-017-6627-4>
- Ben Slimene, E., Lassabatere, L., Šimůnek, J., Winiarski, T., Gourdon, R., 2017. The role of heterogeneous lithology in a glaciofluvial deposit on unsaturated preferential flow – a numerical study. *Journal of Hydrology and Hydromechanics* 65, 209–221. <https://doi.org/10.1515/johh-2017-0004>
- Beven, K., Germann, P., 2013. Macropores and water flow in soils revisited: REVIEW. *Water Resources Research* 49, 3071–3092. <https://doi.org/10.1002/wrcr.20156>
- Birken, R., Versteeg, R., 2000. Use of four-dimensional ground penetrating radar and advanced visualization methods to determine subsurface fluid migration. *Journal of Applied Geophysics* 43, 215–226. [https://doi.org/10.1016/S0926-9851\(99\)00060-9](https://doi.org/10.1016/S0926-9851(99)00060-9)
- Cey, E.E., Rudolph, D.L., 2009. Field study of macropore flow processes using tension infiltration of a dye tracer in partially saturated soils. *Hydrological Processes* 23, 1768–1779. <https://doi.org/10.1002/hyp.7302>
- Concialdi, P., Di Prima, S., Bhandari, H.M., Stewart, R.D., Abou Najm, M.R., Lal Gaur, M., Angulo-Jaramillo, R., Lassabatere, L., 2020. An open-source instrumentation package for intensive soil hydraulic characterization. *Journal of Hydrology* 582. <https://doi.org/10.1016/j.jhydrol.2019.124492>
- Coutinho, A.P., Lassabatere, L., Winiarski, T., Cabral, J.J. da S.P., Antonino, A.C.D., Angulo-Jaramillo, R., 2015. Vadose Zone Heterogeneity Effect on Unsaturated Water Flow Modeling at Meso-Scale. *Journal of Water Resource and Protection* 07, 353–368. <https://doi.org/10.4236/jwarp.2015.74028>
- Di Prima, S., 2019. An open source instrumentation package for intensive soil hydraulic characterization [<https://www.youtube.com/watch?v=KW1zLcuDQg8>].
- Di Prima, S., 2015. Automated single ring infiltrometer with a low-cost microcontroller circuit. *Computers and Electronics in Agriculture* 118, 390–395. <https://doi.org/10.1016/j.compag.2015.09.022>
- Di Prima, S., Castellini, M., Majdi R. Abou Najm, Stewart, R.D., Angulo-Jaramillo, R., Winiarski, T., Lassabatere, L., 2019. Experimental assessment of a new comprehensive model for single ring infiltration data. *Journal of Hydrology* 573, 937–951. <https://doi.org/10.1016/j.jhydrol.2019.03.077>
- Di Prima, S., Concialdi, P., Lassabatere, L., Angulo-Jaramillo, R., Pirastru, M., Cerdà, A., Keesstra, S., 2018. Laboratory testing of Beerkan infiltration experiments for assessing the role of soil sealing on water infiltration. *CATENA* 167, 373–384. <https://doi.org/10.1016/j.catena.2018.05.013>
- Di Prima, S., Lassabatere, L., Bagarello, V., Iovino, M., Angulo-Jaramillo, R., 2016. Testing a new automated single ring infiltrometer for Beerkan infiltration experiments. *Geoderma* 262, 20–34. <https://doi.org/10.1016/j.geoderma.2015.08.006>
- Fletcher, T.D., Shuster, W., Hunt, W.F., Ashley, R., Butler, D., Arthur, S., Trowsdale, S., Barraud, S., Semadeni-Davies, A., Bertrand-Krajewski, J.-L., Mikkelsen, P.S., Rivard, G., Uhl, M., Dagenais, D., Viklander, M., 2015. SUDS, LID, BMPs, WSUD and more – The evolution and application of terminology surrounding urban drainage. *Urban Water Journal* 12, 525–542. <https://doi.org/10.1080/1573062X.2014.916314>
- Gerke, K.M., Sidle, R.C., Mallants, D., 2015. Preferential flow mechanisms identified from staining experiments in forested hillslopes: Preferential Flow Mechanisms Identified from Staining Experiments. *Hydrological Processes* 29, 4562–4578. <https://doi.org/10.1002/hyp.10468>
- Goutaland, D., Winiarski, T., Dubé, J.-S., Bièvre, G., Buoncristiani, J.-F., Chouteau, M., Giroux, B., 2008. Hydrostratigraphic Characterization of Glaciofluvial Deposits Underlying an Infiltration Basin Using Ground Penetrating Radar. *Vadose Zone Journal* 7, 194. <https://doi.org/10.2136/vzj2007.0003>
- Goutaland, D., Winiarski, T., Lassabatere, L., Dubé, J.S., Angulo-Jaramillo, R., 2013. Sedimentary and hydraulic characterization of a heterogeneous glaciofluvial deposit: Application to the modeling of unsaturated flow. *Engineering Geology* 166, 127–139. <https://doi.org/10.1016/j.enggeo.2013.09.006>
- Guo, L., Chen, J., Lin, H., 2014. Subsurface lateral preferential flow network revealed by time-lapse ground-penetrating radar in a hillslope. *Water Resources Research* 50, 9127–9147. <https://doi.org/10.1002/2013WR014603>
- Guo, L., Lin, H., Fan, B., Nyquist, J., Toran, L., Mount, G.J., 2019. Preferential flow through shallow fractured bedrock and a 3D fill-and-spill model of hillslope subsurface hydrology. *Journal of Hydrology* 576, 430–442. <https://doi.org/10.1016/j.jhydrol.2019.06.070>
- Guo, L., Mount, G.J., Hudson, S., Lin, H., Levina, D., 2020. Pairing geophysical techniques improves understanding of the near-surface Critical Zone: Visualization of preferential routing of stemflow along coarse roots. *Geoderma* 357, 113953. <https://doi.org/10.1016/j.geoderma.2019.113953>
- Harari, Z., 1996. Ground-penetrating radar (GPR) for imaging stratigraphic features and groundwater in sand dunes. *Journal of Applied Geophysics* 36, 43–52. [https://doi.org/10.1016/S0926-9851\(96\)00031-6](https://doi.org/10.1016/S0926-9851(96)00031-6)
- Holden, J., 2004. Hydrological connectivity of soil pipes determined by ground-penetrating radar tracer detection. *Earth Surface Processes and Landforms* 29, 437–442. <https://doi.org/10.1002/esp.1039>
- Jackisch, C., Angermann, L., Allroggen, N., Sprenger, M., Blume, T., Tronicke, J., Zehe, E., 2017. Form and function in hillslope hydrology: in situ imaging and characterization of flow-relevant structures. *Hydrology and Earth System Sciences* 21, 3749–3775. <https://doi.org/10.5194/hess-21-3749-2017>
- Jardine, P.M., Wilson, G.V., Luxmoore, R.J., McCarthy, J.F., 1989. Transport of Inorganic and Natural Organic Tracers Through an Isolated Pedon in a Forest Watershed. *Soil Science Society of America Journal* 53, 317. <https://doi.org/10.2136/sssaj1989.03615995005300020001x>
- Klenk, P., Jaumann, S., Roth, K., 2015. Monitoring infiltration processes with high-resolution surface-based Ground-Penetrating Radar. *Hydrol. Earth Syst. Sci. Discuss.* 12, 12215–12246. <https://doi.org/10.5194/hessd-12-12215-2015>
- Kodešová, R., Němeček, K., Kodeš, V., Žigová, A., 2012. Using Dye Tracer for Visualization of Preferential Flow at Macro- and Microscales. *Vadose Zone Journal* 11, 0. <https://doi.org/10.2136/vzj2011.0088>
- Köhne, J.M., Gerke, H.H., 2005. Spatial and temporal dynamics of preferential bromide movement towards a tile drain. *Vadose Zone Journal* 4, 79–88.
- Kung, K.-J.S., 1990. Preferential flow in a sandy vadose zone: 1. Field observation. *Geoderma* 46, 51–58. [https://doi.org/10.1016/0016-7061\(90\)90006-U](https://doi.org/10.1016/0016-7061(90)90006-U)
- Kung, K.-J.S., Donohue, S.V., 1991. Improved Solute-Sampling Protocol in a Sandy Vadose Zone Using Ground-Penetrating Radar. *Soil Science Society of America Journal* 55, 1543. <https://doi.org/10.2136/sssaj1991.03615995005500060007x>
- Lange-Athinodorou, E., El-Raouf, A.A., Ullmann, T., Trappe, J., Meister, J., Baumhauer, R., 2019. The sacred canals of the Temple of Bastet at Bubastis (Egypt): New findings from geomorphological investigations and Electrical Resistivity Tomography (ERT). *Journal of Archaeological Science: Reports* 26, 101910. <https://doi.org/10.1016/j.jasrep.2019.101910>
- Lassabatere, L., Angulo-Jaramillo, R., Goutaland, D., Letellier, L., Gaudet, J.P., Winiarski, T., Delolme, C., 2010. Effect of the settlement of sediments on water infiltration in two urban infiltration basins. *Geoderma* 156, 316–325. <https://doi.org/10.1016/j.geoderma.2010.02.031>
- Lassabatere, L., Angulo-Jaramillo, R., Soria Ugalde, J.M., Cuenca, R., Braud, I., Haverkamp, R., 2006. Beerkan estimation of soil transfer parameters through infiltration experiments – BEST. *Soil Science Society of America Journal* 70, 521. <https://doi.org/10.2136/sssaj2005.0026>
- Lassabatere, L., Di Prima, S., Angulo-Jaramillo, R., Keesstra, S., Salesa, D., 2019a. Beerkan multi-runs for characterizing water infiltration and spatial variability of soil hydraulic properties across scales. *Hydrological Sciences Journal* 64, 165–178. <https://doi.org/10.1080/02626667.2018.1560448>
- Lassabatere, L., Di Prima, S., Bouarafa, S., Iovino, M., Bagarello, V., Angulo-Jaramillo, R., 2019b. BEST-2K Method for Characterizing Dual-Permeability Unsaturated Soils with Ponded and Tension Infiltrometers. *Vadose Zone Journal* 18. <https://doi.org/10.2136/vzj2018.06.0124>
- Di Prima, S., Winiarski, T., Angulo-Jaramillo, R., Stewart, R.D., Castellini, M., Abou Najm, M.R., Ventrella, D., Pirastru, M., Giadrossich, F., Lassabatere, L., 2020. Detecting infiltrated water and preferential flow pathways through time-lapse ground-penetrating radar surveys. *Science of the Total Environment*. <https://doi.org/10.1016/j.scitotenv.2020.138511>

- Lassabatere, L., Spadini, L., Delolme, C., Février, L., Galvez Cloutier, R., Winiarski, T., 2007. Concomitant Zn–Cd and Pb retention in a carbonated fluvio-glacial deposit under both static and dynamic conditions. *Chemosphere* 69, 1499–1508. <https://doi.org/10.1016/j.chemosphere.2007.04.053>
- Lassabatere, L., Winiarski, T., Galvez-Cloutier, R., 2004. Retention of Three Heavy Metals (Zn, Pb, and Cd) in a Calcareous Soil Controlled by the Modification of Flow with Geotextiles. *Environmental Science & Technology* 38, 4215–4221. <https://doi.org/10.1021/es035029s>
- Lassabatere, L., Yilmaz, D., Peyrard, X., Peyneau, P.E., Lenoir, T., Šimůnek, J., Angulo-Jaramillo, R., 2014. New Analytical Model for Cumulative Infiltration into Dual-Permeability Soils. *Vadose Zone Journal* 0, 0. <https://doi.org/10.2136/vzj2013.10.0181>
- Longo, V., Testone, V., Oggiano, G., Testa, A., 2014. Prospecting for clay minerals within volcanic successions: Application of electrical resistivity tomography to characterise bentonite deposits in northern Sardinia (Italy). *Journal of Applied Geophysics* 111, 21–32. <https://doi.org/10.1016/j.jappgeo.2014.09.014>
- Luo, Z., Niu, J., Xie, B., Zhang, L., Chen, X., Berndtsson, R., Du, J., Ao, J., Yang, L., Zhu, S., 2019. Influence of Root Distribution on Preferential Flow in Deciduous and Coniferous Forest Soils. *Forests* 10, 986. <https://doi.org/10.3390/f10110986>
- Moncef, H., Hedi, D., Jelloul, B., Mohamed, M., 2002. Approach for predicting the wetting front depth beneath a surface point source: theory and numerical aspect. *Irrig. and Drain.* 51, 347–360. <https://doi.org/10.1002/ird.60>
- Regalado, C.M., Ritter, A., Álvarez-Benedí, J., Muñoz-Carpena, R., 2005. Simplified Method to Estimate the Green–Ampt Wetting Front Suction and Soil Sorptivity with the Philip–Dunne Falling-Head Permeameter. *Vadose Zone Journal* 4, 291. <https://doi.org/10.2136/vzj2004.0103>
- RockWare, Inc., 2015. *RockWorks17 User's Manual*. URL <https://www.rockware.com/downloads/documentation/rockworks/rockworks17.pdf>.
- Sander, T., Gerke, H.H., 2007. Preferential Flow Patterns in Paddy Fields Using a Dye Tracer. *Vadose Zone Journal* 6, 105. <https://doi.org/10.2136/vzj2006.0035>
- Stewart, R.D., 2019. A Generalized Analytical Solution for Preferential Infiltration and Wetting. *Vadose Zone Journal* 18. <https://doi.org/10.2136/vzj2018.08.0148>
- Stewart, R.D., Najm, M.R.A., Rupp, D.E., Selker, J.S., 2014. Nondestructive Quantification of Macropore Volume using Shear-Thinning Fluid. *Soil Science Society of America Journal* 78, 445–453. <https://doi.org/10.2136/sssaj2013.08.0346>
- Trinks, I., Stümpel, H., Wachsmuth, D., 2001. Monitoring water flow in the unsaturated zone using georadar. *First Break* 19, 679–684. <https://doi.org/10.1046/j.1365-2397.2001.00228.x>
- Truss, S., Grasmueck, M., Vega, S., Viggiano, D.A., 2007. Imaging rainfall drainage within the Miami oolitic limestone using high-resolution time-lapse ground-penetrating radar: IMAGING DRAINAGE USING TIME-LAPSE GPR. *Water Resour. Res.* 43. <https://doi.org/10.1029/2005WR004395>
- Weiler, M., Naef, F., 2003. An experimental tracer study of the role of macropores in infiltration in grassland soils. *Hydrol. Process.* 17, 477–493. <https://doi.org/10.1002/hyp.1136>
- Winiarski, T., Bedell, J.-P., Delolme, C., Perrodin, Y., 2006. The impact of stormwater on a soil profile in an infiltration basin. *Hydrogeology Journal* 14, 1244–1251. <https://doi.org/10.1007/s10040-006-0073-9>
- Yilmaz, D., Lassabatere, L., Angulo-Jaramillo, R., Deneele, D., Legret, M., 2010. Hydrodynamic Characterization of Basic Oxygen Furnace Slag through an Adapted BEST Method. *Vadose Zone Journal* 9, 107. <https://doi.org/10.2136/vzj2009.0039>
- Yilmaz, D., Lassabatere, L., Deneele, D., Angulo-Jaramillo, R., Legret, M., 2013. Influence of Carbonation on the Microstructure and Hydraulic Properties of a Basic Oxygen Furnace Slag. *Vadose Zone Journal* 12, 0. <https://doi.org/10.2136/vzj2012.0121>